https://doi.org/10.5194/egusphere-2026-891
Preprint. Discussion started: 18 February 2026
© Author(s) 2026. CC BY 4.0 License.

Satellite observations reveal heterogeneous atmospheric composition responses to rapid emission changes

Zeyu Yang[1,2], Fan Cheng[1,3,4], Jian Gao[5], Huan Liu[2], Jing Wei[1*]

1. MEEKL-AERM, College of Environmental Sciences and Engineering, Institute of Tibetan Plateau, and Center for Environment and Health, Peking University, Beijing, China
2. School of Environment, Tsinghua University, Beijing, China
3. School of Environmental and Sustainable Engineering, Eastern Institute of Technology Ningbo, Ningbo, China
4. School of Environmental Science and Engineering, Shanghai Jiao Tong University, Shanghai, China
5. Chinese Research Academy of Environmental Sciences, Beijing, China

*Correspondence: Jing Wei (jingwei@pku.edu.cn)

Abstract

We developed a unified machine learning framework to retrieve daily, 1 km resolution, gap-free concentrations of six major atmospheric pollutants across China, providing a consistent basis for quantifying atmospheric composition responses to rapid emission perturbations. Our results reveal pronounced spatiotemporal variability across pollutant species, with recovery times ranging from two to eight weeks following abrupt emission reductions. Most air pollutants, such as particulate matter (PM) and NO_2, exhibited rapid declines and subsequent rebounds, consistent with changes in anthropogenic emissions, whereas O_3 showed the opposite response, reflecting nonlinear photochemical processes under reduced NO_x conditions. In contrast, SO_2 and CO displayed more sustained decreases, indicating longer-term structural changes in combustion-related sources. By integrating explainable artificial intelligence with atmospheric predictors, we disentangle meteorological and emission-driven contributions to the variability of secondary pollutants across spatial scales. In Wuhan, reduced anthropogenic emissions contributed to a 22% decrease in $PM_{2.5}$ during the emission-reduction period, whereas enhanced atmospheric oxidation associated with

https://doi.org/10.5194/egusphere-2026-891
Preprint. Discussion started: 18 February 2026
© Author(s) 2026. CC BY 4.0 License.

meteorological variability led to a 40% increase in O_3. During the subsequent recovery phase, meteorological factors dominated interannual variability, driving a 16% rebound in $PM_{2.5}$ but a 5% decline in O_3. These findings elucidate the chemical and physical mechanisms governing atmospheric composition under rapid perturbations in emissions and underscore the nonlinear coupling among primary emissions, secondary formation, and meteorological processes.

1. Introduction

Rapid and large-scale changes in anthropogenic emissions during the coronavirus disease 2019 pandemic provide natural experiments for understanding the chemical and physical processes governing atmospheric composition. The abrupt reduction in human activities in China during early 2020 led to substantial short-term emission perturbations (Venter et al., 2020; Cooper et al., 2022; Wei et al., 2023a, 2023b; Zhu et al., 2021), offering a unique opportunity to investigate the response of multiple atmospheric pollutants to altered precursor emissions. As restrictions eased and human activities resumed, pollution levels responded accordingly. These changes occurred against the backdrop of long-term emission control policies, including the Blue Sky Protection Campaign (2018–2020) and the 14th Five-Year Plan (2021–2025), which further influenced atmospheric dynamics. However, the heterogeneous responses of different pollutant species and the mechanisms governing their evolution during subsequent emission recovery phases remain poorly understood.

A growing body of research has examined pollutant changes during the emission-reduction period in China. For example, Wang & Zhang (2020) observed significant decreases in ground-based measurements of six major ambient air pollutants at the provincial level under strict activity restrictions, with 65% of provinces showing normalized $PM_{2.5}$ and PM_{10} concentrations below 80% and 70%, respectively, relative to historical levels. Cooper et al. (2022) found that surface NO_2 concentrations derived from TROPOMI data decreased by more than 10 ppbv in February in China, with declines persisting in eastern urban areas through April. These reductions were equivalent to more than three years of typical declines, and regions with the largest NO_2 decreases also showed greater local reductions in $PM_{2.5}$ levels. In contrast, Wei et al. (2022a) reported that surface O_3 concentrations, derived from satellite data using machine learning, increased substantially across eastern China during the lockdown, with relative changes exceeding 40% in epidemic-hit areas,

https://doi.org/10.5194/egusphere-2026-891
Preprint. Discussion started: 18 February 2026
© Author(s) 2026. CC BY 4.0 License.

such as Hubei province and surrounding regions. Geng et al. (2024) found that emission reductions from industrial and socioeconomic activity led to a 14% decrease in $PM_{2.5}$ exposure levels from January to April, simulated by the WRF/CMAQ model.

While short-term lockdowns initially had a significant impact and may have lasting effects, the subsequent rebound in anthropogenic emissions as restrictions eased could influence pollutant levels in various ways in the following years. However, the evolution of atmospheric composition during these emission recovery phases has received comparatively less attention. Wang & Yang (2021) reported a varying-degree rebound in ground-measured air pollutants during April–September 2020 in nine Chinese cities, particularly for PM_{10} and NO_2, which increased by 44% and 87% in September, respectively. They also observed a notably slower decline compared to the same period from 2017 to 2019, with concentrations occasionally exceeding the multi-year average. Guo et al. (2021) found that mean pollution levels and concentrations of six individual pollutants during May–October 2021 were 15% and 8–38% lower, respectively, than those of the same period in 2020 in the Beijing-Tianjin-Tangshan region. Bhatti et al. (2022) observed increased air pollution during January–May 2021 in Jiangsu province, with PM_{10} and NO_2 rising by 23% and 16%, respectively, resulting in a 3% increase in the air quality index, according to the weather post report. Feng et al. (2022) reported that $PM_{2.5}$ concentrations increased by 22.3 μg m^{-3} in former lockdown cities during April–October 2020 compared to January–February 2020, while national levels remained lower than pre-lockdown 2019 values by 8.8–11.2 μg m^{-3}, based on a weather-standardized pollutant dataset.

However, previous studies have largely focused on short-term pollution changes immediately following lockdowns, typically within specific regions and over limited periods, such as the early months of activity resumption. Most studies have also emphasized individual pollutants, such as $PM_{2.5}$ or NO_2, which reflects only the most severe pollutant at a given time. Furthermore, many analyses are based on heterogeneous datasets, particularly from ground-based measurements with limited spatial coverage due to the uneven distribution of monitoring stations in China. These limitations constrain the generalizability of findings and leave a critical gap in understanding nationwide pollution trends, especially in urban areas, where exposure and health risks are more pronounced. To date, no comprehensive assessment has fully captured the collective behavior of

https://doi.org/10.5194/egusphere-2026-891
Preprint. Discussion started: 18 February 2026
© Author(s) 2026. CC BY 4.0 License.

multiple air pollutants, particularly at fine spatial scales, where interactions among pollutants are more complex.

How has atmospheric composition evolved before, during, and after periods of rapid emission changes? What shifts have occurred in individual and composite pollutants, and what are the key drivers behind these changes? These questions can be addressed using advanced artificial intelligence (AI) models that leverage large-scale datasets spanning ground-based observations and satellite retrievals. In this study, we developed a state-of-the-art deep learning (DL) model to, for the first time, uniformly estimate six conventional outdoor air pollutants—fine particulate matter ($PM_{2.5}$), coarse particulate matter (PM_{10}), surface ozone (O_3), nitrogen dioxide (NO_2), sulfur dioxide (SO_2), and carbon monoxide (CO), primarily from satellite aerosol and trace gas retrievals at unprecedented spatial (1 km^2) and temporal (daily) resolutions with complete coverage. Using this dataset, we investigate the spatiotemporal evolution of atmospheric composition across emission reduction and recovery phases and quantify the relative contributions of anthropogenic emissions and meteorological processes through explainable artificial intelligence. By examining coupled responses of primary and secondary pollutants across spatial scales, this study provides process-level insights into how rapid emission perturbations modulate atmospheric chemistry and composition.

2. Materials and Methods

2.1 Air pollutant modeling and validation

Ambient pollutant concentration data were obtained from the ChinaHighAirPollutants (CHAP) database, developed by our team and extensively applied in environmental health studies. The CHAP database integrates ground observations, satellite retrievals, and chemical transport model simulations, addressing gaps in satellite data while capturing non-linear relationships between satellite column retrievals and surface pollutant concentrations through advanced spatiotemporal artificial intelligence (AI) models. This integration produces a long-term daily dataset with full spatial coverage and high spatiotemporal resolution. In this study, six conventional air pollutants from 2019 to 2022 were analyzed, including two particulate species ($PM_{2.5}$ and PM_{10}) and four gaseous pollutants (i.e., O_3, NO_2, SO_2, and CO), all uniformly resolved at 1 km spatial resolution on a daily basis.

https://doi.org/10.5194/egusphere-2026-891
Preprint. Discussion started: 18 February 2026
© Author(s) 2026. CC BY 4.0 License.

These AQ products are derived from the latest version, featuring significant enhancements to key input variables within a unified AI framework—the four-dimensional spatiotemporal deep forest (4D-STDF) model—which aims to minimize inconsistencies across datasets and to ensure higher accuracy and reliability. A key improvement over the original deep forest model is the incorporation of spatiotemporal information to enhance performance, achieved by accounting for unequal spatial autocorrelations and differences using 3 spherical coordinates in Euclidean space, $Ps \sim [S_1, S_2, S_3] = [\sin\left(2\pi\frac{Lon}{360}\right), \cos\left(2\pi\frac{Lon}{360}\right)\sin\left(2\pi\frac{Lat}{180}\right), \cos\left(2\pi\frac{Lon}{360}\right)\cos\left(2\pi\frac{Lat}{180}\right)]$, along with 3 helix-shaped trigonometric vectors, i.e., $Pt \sim [T_1, T_2, T_3] = [\frac{DOY}{N}, \cos\left(2\pi\frac{DOY}{N}\right), \sin\left(2\pi\frac{DOY}{N}\right)]$, to capture daily variations and seasonal cycles in air pollution.

Specifically, $PM_{2.5}$ and PM_{10} were estimated using MODIS MAIAC 1 km AOD products as the primary predictors (Wei et al., 2021a, 2021b), whereas surface concentrations of O_3 (Yang et al., 2025), NO_2 (Wei et al., 2022b), SO_2 (Wei et al., 2023a), and CO (Wei et al., 2023a) were derived from *downscaled 1 km* TROPOMI vertical column density products utilizing a geostatistical technique (Cersosimo et al., 2020) implemented on the Google Earth Engine platform. Table S1 provides a summary of all data utilized for pollutant modeling in this study.

During the modeling process, ground-based measurements of each air pollutant served as the target variables, while predictors were specifically tailored for each pollutant. For $PM_{2.5}$, key input variables included MODIS MAIAC gap-filled AOD, GEOS-CF $PM_{2.5}$ simulations, and anthropogenic emissions (e.g., $PM_{2.5}$, NH_4, NO_x, SO_2, CO, and VOCs) from the daily 1 km anthropogenic emissions provided by Tsinghua's Air Benefit and Cost and Attainment Assessment System–Emission Inventory (ABaCAS-EI). Additional auxiliary variables influencing $PM_{2.5}$ concentrations included ERA5 meteorological factors such as boundary-layer height (BLH), air temperature (TEM), relative humidity (RH), surface pressure (SP), total precipitation (TP), total evaporation (ET), wind speed (WS), and wind direction (WD). Further predictors comprised the normalized difference vegetation index (NDVI), digital elevation model (DEM), population density (POD), nighttime lights (NTL), and spatiotemporal terms (*Ps* and *Pt*):

https://doi.org/10.5194/egusphere-2026-891
Preprint. Discussion started: 18 February 2026
© Author(s) 2026. CC BY 4.0 License.

$$PM_{2.5} \sim f_{\text{4D-STDF}}(MAIAC_{AOD}, GEOS_{PM_{2.5}}, \text{ABaCAS}_{PM_{2.5},NH_4,NO_x,SO_2,CO,VOCs}, ERA5_{BLH,TEM,SP,RH,TP,ET,WS,WD}, NDVI, DEM, POD, NTL, P_s, P_t) \quad (1)$$

For PM_{10}, the input variables included MODIS MAIAC gap-filled AOD, CAMS PM_{10} simulations, and ABaCAS-EI PM_{10} anthropogenic emissions, along with the same meteorological, surface-related, population-related, and spatiotemporal variables used for $PM_{2.5}$, as expressed below:

$$PM_{10} \sim f_{\text{4D-STDF}}(MAIAC_{AOD}, CAMS_{PM_{10}}, \text{ABaCAS}_{PM_{10}}, ERA5_{BLH,TEM,SP,RH,TP,ET,WS,WD}, NDVI, DEM, POD, NTL, P_s, P_t) \quad (2)$$

For surface NO_2, the input variables included the TROPOMI gap-filled tropospheric NO_2 column, GEOS-CF surface NO_2 simulations, and ABaCAS-EI NO_x anthropogenic emissions, along with the same meteorological, surface-, population-related, and spatiotemporal variables for PM:

$$NO_2 \sim f_{\text{4D-STDF}}(TROPOMI_{NO_2}, GEOS_{NO_2}, \text{ABaCAS}_{NO_x}, ERA5_{BLH,TEM,SP,RH,TP,ET,WS,WD}, NDVI, DEM, POD, NTL, P_s, P_t) \quad (3)$$

For surface SO_2, the main predictors included the TROPOMI gap-filled total SO_2 column, GEOS-CF surface SO_2 simulations, and ABaCAS-EI SO_2 anthropogenic emissions, along with the same auxiliary variables used for NO_2:

$$SO_2 \sim f_{\text{4D-STDF}}(TROPOMI_{SO_2}, GEOS_{SO_2}, \text{ABaCAS}_{SO_2}, ERA5_{BLH,TEM,SP,RH,TP,ET,WS,WD}, NDVI, DEM, POD, NTL, P_s, P_t) \quad (4)$$

For surface CO, the main predictors include the TROPOMI gap-filled total CO column, GEOS-CF surface CO simulations, and ABaCAS-EI CO anthropogenic emissions, , along with the same auxiliary data used for NO_2 and SO_2:

$$CO \sim f_{\text{4D-STDF}}(TROPOMI_{CO}, GEOS_{CO}, \text{ABaCAS}_{CO}, ERA5_{BLH,TEM,SP,RH,TP,ET,WS,WD}, NDVI, DEM, POD, NTL, P_s, P_t) \quad (5)$$

https://doi.org/10.5194/egusphere-2026-891
Preprint. Discussion started: 18 February 2026
© Author(s) 2026. CC BY 4.0 License.

For surface O_3, the main predictors included the TROPOMI gap-filled tropospheric NO_2 and HCHO columns, GEOS-CF surface O_3 simulations, and ABaCAS-EI anthropogenic emissions of NO_x, VOCs, and CO. Additionally, two key factors influencing photochemical reactions for ozone formation—satellite-derived surface downward shortwave radiation (DSR) and land surface temperature (LST) products—were integrated. The model also included the same auxiliary variables used for NO_2, SO_2, and CO:

$$O_3 \sim f_{4D-STDF}(TROPOMI_{NO_2,HCHO}, GEOS_{O_3}, \mathrm{ABaCAS}_{NO_x,VOCs,CO}, DSR, LST, ERA5_{BLH,SP,RH,TP,ET,WS,WD}, NDVI, DEM, POD, NTL, P_s, P_t) \quad (6)$$

These estimated daily AQ data are comprehensively validated against surface measurements from over 1,700 ground-based monitoring stations across China, as reported by the China National Environmental Monitoring Centre (MEE, 2018). The evaluation utilizes three commonly used independent validation approaches for AI regression tasks: out-of-sample, out-of-station, and out-of-day ten-fold cross-validation (10-CV). These techniques are used to assess overall accuracy, spatial predictive accuracy, and temporal predictive accuracy, respectively. The latter two methods are specifically designed to evaluate the AI model's performance in predicting AQ data for areas and days without ground observations (Wei et al., 2023b, 2023c, 2023d).

2.2 Air pollution assessment method

The Air Quality Index (AQI) conveys daily pollution levels and is divided into six categories representing different degrees of public exposure: Good (0–50), Moderate (51–100), Unhealthy for Sensitive Groups (101–150), Unhealthy (151–200), Very Unhealthy (201–300), and Hazardous (301–500). The index is calculated by determining the Individual Air Quality Index (IAQI) for six key air pollutants: fine and coarse particulate matter ($PM_{2.5}$ and PM_{10}), and gaseous pollutants, including ozone (O_3), nitrogen dioxide (NO_2), sulfur dioxide (SO_2), and carbon monoxide (CO):

$$IAQI_p = \left(C_p - C_{p,l}\right) \times \frac{IAQI_{p,j} - IAQI_{p,j-1}}{C_{p,h} - C_{p,l}} + IAQI_{p,l} \quad (7)$$

where $IAQI_p$ represents the IAQI of pollutant p; C_p is the surface concentration of pollutant p. The thresholds $C_{p,l}$ and $C_{p,h}$ are defined as the lower and upper surface concentration limits for pollutant

https://doi.org/10.5194/egusphere-2026-891
Preprint. Discussion started: 18 February 2026
© Author(s) 2026. CC BY 4.0 License.

p, respectively, selected based on proximity to C_p, while $IAQI_{p,j}$ and $IAQI_{p,j-1}$ correspond to IAQI values for these limits (Table S2).

In this study, we employed the refined Aggregated Air Quality Index (AAQI), which considers the combined effects of multiple key pollutants (Kyrkilis et al., 2007), offering a more comprehensive assessment by integrating exposure from various pollutant sources:

$$AAQI = \left(\sum_{i=1}^{n}\left(IAQI_p\right)^{\rho}\right)^{\frac{I}{\rho}} \quad (8)$$

where ρ is a constant that modulates the aggregation effect of individual IAQIs. Here, we set ρ to 2, allowing us to consider the combined effects of each pollutant while still emphasizing the impact of certain more severe pollutants in China (Hu et al., 2015). Similarly, the AAQI values are also capped at 500 to avoid skewing the assessment.

2.3 Air pollution response analysis method

To comprehensively evaluate the impact of abrupt emission changes, the study period was divided into three distinct phases: the pre-reduction period (2019), the reduction period (2020), and the recovery period (2021–2022). First, air pollutant data were adjusted to minimize the influence of short-term meteorological variations using our previously developed method. Then, Seasonal-Trend Decomposition (Cleveland et al., 1990) was applied to separate short-term fluctuations and seasonal effects, ensuring that the observed trends reflect true changes in pollutant levels:

$$y_t = T_t + S_t + R_t \quad (9)$$

where y_t is the observed time series, T_t is the trend component, S_t is the seasonal component, and R_t is the residual (noise) component. The Seasonal and Trend components are extracted using the Locally estimated scatterplot smoothing (STL) model, a nonparametric regression method that fits a smooth curve to the data with local polynomial regression within a moving window and assigns weights based on the distance from the window's centre:

https://doi.org/10.5194/egusphere-2026-891
Preprint. Discussion started: 18 February 2026
© Author(s) 2026. CC BY 4.0 License.

$$min \sum_i \omega_i (y_i - (b_0 + b_1(x_i - x) + \cdots))^2 \quad (10)$$

where ω_i is the weight determined by a kernel function (e.g., tricubic kernel) for the smoothed value at a point x using the weighted least squares method.

The response duration—defined as the time required for pollutants to return to baseline levels after abrupt emission changes—was determined by identifying the start and end dates of emission perturbation phases based on intersections of pollutant levels between pre-reduction and reduction periods. Using this response period, changes in pollutant levels across different emission phases were quantified. To establish a common temporal baseline across years, the Chinese New Year was set as the start of the year, mitigating holiday-related impacts on pollutant levels.

2.4 Driving factor analysis method

Considering that certain factors (e.g., land use and surface elevation) remain relatively stable over short timescales, the drivers of air pollution were classified into meteorological and anthropogenic factors, with a focus on two major secondary pollutants. For $PM_{2.5}$, anthropogenic factors included surface concentrations of SO_2, NO_2, and CO from the CHAP daily AQ datasets, as well as surface VOCs from the CAMS reanalysis. For surface O_3, major precursors included CHAP daily surface NO_2 and CO concentrations together with CAMS surface VOC concentrations. Meteorological variables were sourced from the ERA5 reanalysis dataset (Hersbach et al., 2020; Muñoz-Sabater et al., 2021) and included boundary-layer height (BLH), relative humidity (RH), surface pressure (SP), total precipitation (TP), air temperature (TEM), and wind speed and direction for $PM_{2.5}$. For O_3, additional variables related to photochemical reactions were incorporated, including MODIS daily surface downward shortwave radiation (DSR) products (Yang et al., 2025) and ERA5 daily surface sensible heat flux and total cloud cover.

To identify the drivers of pollution changes across different emission phases, we employed SHapley Additive exPlanations (SHAP; Antwarg et al., 2021), an advanced eXplainable Artificial Intelligence (XAI) method. SHAP provides a flexible and interpretable framework for ML/DL

https://doi.org/10.5194/egusphere-2026-891
Preprint. Discussion started: 18 February 2026
© Author(s) 2026. CC BY 4.0 License.

modeling, especially when spatial and non-spatial effects interact (Cheng et al., 2025; Li, 2022; Wei et al., 2024). Key features of SHAP include consistent allocation of feature contributions and the ability to capture complex interactions while maintaining global and local interpretability. The contribution of each factor can be expressed as:

$$\phi_f = \frac{1}{N}\sum_{k=1}^{N}\left|\sum_{S \subseteq N}\frac{|S|!\,(|N| - |S| - 1)!}{|N|!}[f(S \cup \{i\}) - f(S))]\right| \quad (11)$$

where ϕ_f represents the SHAP value for a given feature, quantifying its average contribution to the model's prediction. N is the total number of samples, and S is a subset of features with $|S|$ as its size, and $|N|$ as the total number of features. The weight factor $\frac{|S|!(|N|-|S|-1)!}{|N|!}$ measures the importance of the subset S within all possible feature permutations. $f(S \cup \{i\})$ denotes the model output when feature i is included, while $f(S)$ represents the output when it is excluded.

In addition to SHAP, the traditional multiple linear regression (MLR) method was performed for comparison, using standardized regression coefficients to evaluate the average contribution of each factor. The same set of input variables used in the XAI analysis was applied, along with additional feature testing to address multicollinearity issues (Tables S3 and S4), evaluated using the Variance Inflation Factor (VIF) method (Wei et al., 2022a).

3. Results and Discussion

3.1 Evaluation of space-based air pollutant monitoring

Our developed uniform DL model can effectively daily ambient particulate and gaseous pollutants, demonstrating high sample-based cross-validation coefficients of determination (CV-R^2) [low root mean-square errors (RMSE)] values—0.92 (16.87 μg m^{-3}) for PM_{10}, 0.93 (7.58 μg m^{-3}) for $PM_{2.5}$, 0.94 (11.48 μg m^{-3}) for O_3, 0.87 (6.34 μg m^{-3}) for NO_2, 0.79 (3.93 μg m^{-3}) for SO_2, and 0.80 (0.18 mg m^{-3}) for CO—validated against over 2.2 million ground-based observations collected from 2019 to 2022 at the national scale (Fig. 1). Strong model performance is also observed at individual ground-based monitoring stations across the domain (e.g., 52–99% exhibiting moderate to strong CV-R^2 values > 0.5), particularly in the eastern regions (Fig. S1). Additionally, the model

https://doi.org/10.5194/egusphere-2026-891
Preprint. Discussion started: 18 February 2026
© Author(s) 2026. CC BY 4.0 License.

305 maintains consistent reliability in both spatial and temporal predictions of various air pollutant species across China, with minor declines in station-based and day-based cross-validated R^2 values (ranging from 0.63 to 0.92, and 0.64 to 0.8, respectively) when randomly dropping ground-based monitoring stations and observation days (Figs. S2-S3). These results underscore the strong potential of deep learning in monitoring pollution from space, particularly in areas and on days
310 lacking direct ground measurements. However, the performance of specific trace gas retrievals (e.g., SO_2 and CO) is relatively poorer than that of particulate matter pollutants, primarily due to the weaker signals and reduced sensitivity of satellite observations.

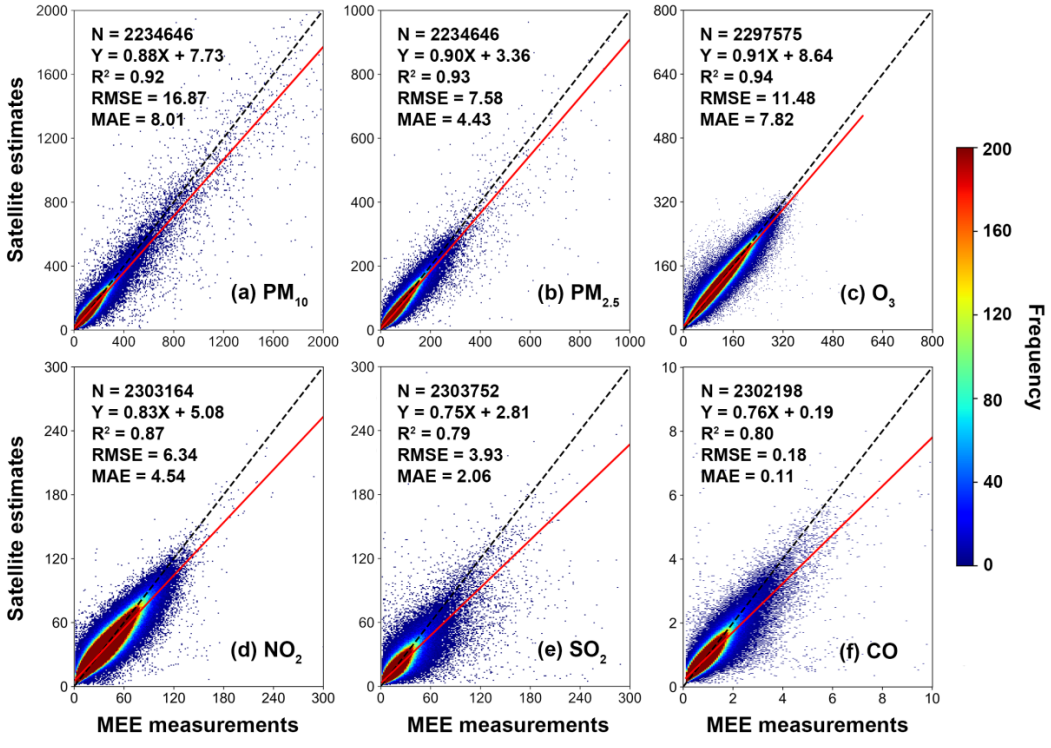

315 **Figure 1. Overall accuracy of daily air pollutant estimates across China.**
Density scatter plots of satellite-derived daily gapless 1-km-resolution concentrations of ambient air pollutants—(a) PM_{10} (μg m^{-3}), (b) $PM_{2.5}$ (μg m^{-3}), (c) O_3 (μg m^{-3}), (d) NO_2 (μg m^{-3}), (e) SO_2 (μg m^{-3}), and (f) CO (mg m^{-3})—using the unified four-dimensional spatiotemporal deep forest (4D-STDF) model against ground-based measurements from all Ministry of Ecology and Environment
320 (MEE) monitoring stations across China from 2019 to 2022, based on the sample-based 10-fold cross-validation approach. The black dashed lines represent the 1:1 reference line, while the red lines indicate the best-fit lines derived from linear regression.

https://doi.org/10.5194/egusphere-2026-891
Preprint. Discussion started: 18 February 2026
© Author(s) 2026. CC BY 4.0 License.

3.2 Impacts of abrupt emission changes on air pollution

Using machine learning, we derived daily, gapless 1-km maps of six ambient air pollutants across China from satellite observations, providing spatially continuous estimates at each location and for each day, particularly in regions lacking ground-based measurements. Figure 2 presents a representative example on 1 January 2020, illustrating pronounced pollutant-specific spatial heterogeneity. Particulate matter exhibits strong regional clustering, with PM_{10} showing elevated concentrations in arid and semi-arid regions of northwestern China, largely influenced by natural dust emissions and surface wind erosion, while $PM_{2.5}$ displays prominent hotspots over major urbanized and industrialized regions such as the North China Plain, the Fenwei Plain, and the Sichuan Basin. These $PM_{2.5}$ enhancements are closely associated with intensive anthropogenic emissions and unfavorable meteorological conditions during winter, including shallow boundary layers and weak ventilation, which promote pollutant accumulation.

In contrast, gaseous pollutants exhibit distinct spatial patterns that reflect differences in emission sources and chemical lifetimes. NO_2 exhibits strong urban-scale gradients and is tightly linked to traffic and industrial combustion sources, whereas SO_2 concentrations are generally low nationwide due to effective emission control policies, with residual enhancements confined to localized industrial regions. CO presents a relatively homogeneous spatial distribution owing to its longer atmospheric lifetime and regional transport. O_3 shows higher concentrations in western and high-altitude regions, while remaining lower in eastern urban areas during winter, reflecting weaker photochemical production and enhanced NO titration. Together, these results highlight the ability of high-resolution, gapless datasets to capture multi-scale characteristics of air pollution and their underlying drivers across China.

https://doi.org/10.5194/egusphere-2026-891
Preprint. Discussion started: 18 February 2026
© Author(s) 2026. CC BY 4.0 License.

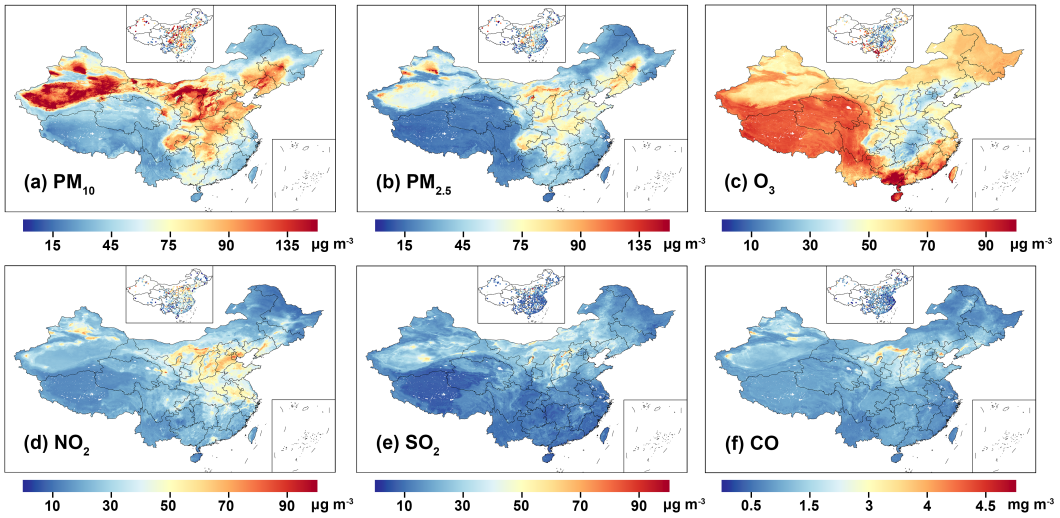

Figure 2. Example of daily 1 km gapless ambient air pollution datasets in China.
A typical example of (a–f) satellite-derived (horizontal resolution = 1 km) gapless surface (a) PM_{10} ($\mu g\ m^{-3}$), (b) $PM_{2.5}$ ($\mu g\ m^{-3}$), (c) O_3 ($\mu g\ m^{-3}$), (d) NO_2 ($\mu g\ m^{-3}$), (e) SO_2 ($\mu g\ m^{-3}$), and (f) CO ($mg\ m^{-3}$) compared with ground measurements on 1 January 2020 in China (inserted upper-middle maps).

These high-resolution pollution datasets enable a detailed examination of short-term pollutant responses to abrupt emission changes (Fig. 3). During the period of stringent emission reductions, most pollutants exhibited substantial declines, although the magnitude and temporal response varied markedly among species. The Individual Air Quality Index (IAQI) for $PM_{2.5}$ showed a sharp decline of 30% over 22 days, while PM_{10} decreased by 15%, taking twice as long—47 days—to return to normal levels. NO_2 experienced the largest drop, dropping by 32% over a 52-day response period, while SO_2 and CO demonstrated moderate reductions of 21% and 19% over 45 and 25 days, respectively, driven by significantly reduced anthropogenic emissions from transportation and industrial sources (Wei et al., 2022b, 2023a). In contrast, O_3 concentrations increased by 18% and exhibited the fastest rebound time (17 days), largely attributable to the substantial reduction in nitrogen oxides (NO_x) emissions under a VOC-limited (NO_x-saturated) chemical regime across much of eastern China (Liu et al., 2021; Wei et al., 2022a). Overall, the AAQI declined by 17% during the most stringent reduction period, indicating widespread improvements in pollution levels across China.

https://doi.org/10.5194/egusphere-2026-891
Preprint. Discussion started: 18 February 2026
© Author(s) 2026. CC BY 4.0 License.

During the subsequent emission recovery phase, pollutant-specific responses varied considerably. Approximately half of the pollutant species showed rebounds consistent with a partial resumption of anthropogenic emissions. NO_2 increased most notably, rising by 25% relative to the reduction phase, reflecting the recovery of traffic and industrial activities. PM_{10} increased by 16%, influenced both by spring dust events and renewed human activities. O_3 exhibited a slight increase of 1%, highlighting the continued complexity of ozone formation driven by changes in precursor emissions, particularly NO_x. In contrast, $PM_{2.5}$ decreased marginally by 1%, suggesting more persistent improvements, while SO_2 and CO decreased by 3% and 8%, respectively, indicating sustained control of primary emissions. Overall, the AAQI increased by 10% during the recovery phase, reflecting a partial rise in pollution levels; however, conditions remained better than pre-reduction levels, with the AAQI still 9% lower on average, particularly for $PM_{2.5}$ (31% reduction) and its major precursors (16–26% reductions). These results suggest that although some benefits diminished as emissions resumed, structural reductions and ongoing policy measures contributed to lasting improvements in air quality.

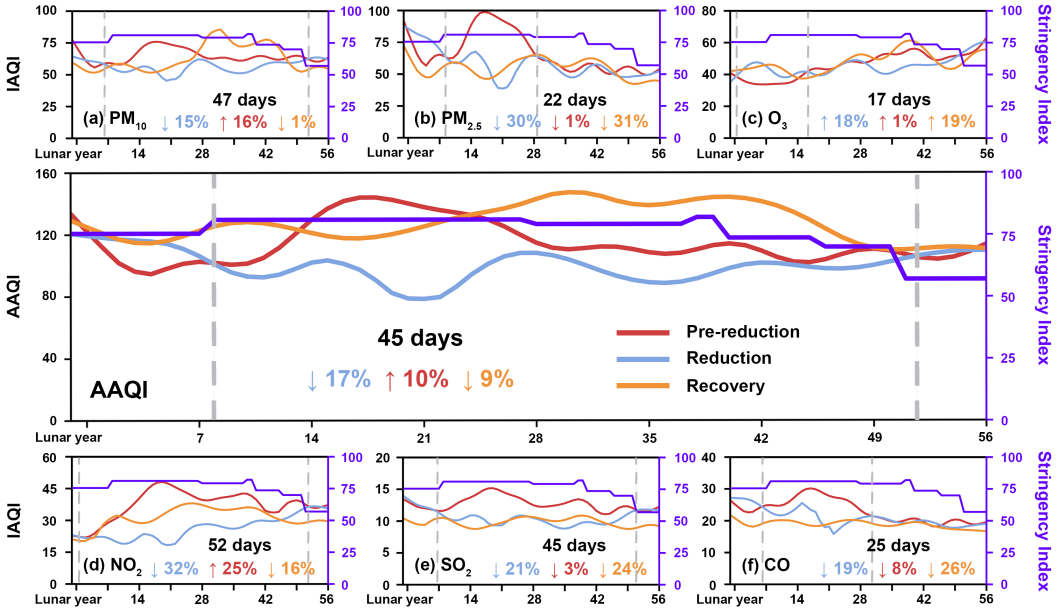

Figure 3. Response of air pollution to emission changes in China.
Time series of daily Aggregated Air Quality Index (AAQI) and Individual Air Quality Index (IAQI) (colored lines) for (a) PM_{10}, (b) $PM_{2.5}$, (c) O_3, (d) NO_2, (e) SO_2, and (f) CO, along with the Oxford Coronavirus Government Response Tracker (OxCGRT) stringency index (purple lines) as a proxy

https://doi.org/10.5194/egusphere-2026-891
Preprint. Discussion started: 18 February 2026
© Author(s) 2026. CC BY 4.0 License.

for emission reduction intensity during the pre-reduction (2019), reduction (2020), and recovery (2021–2022) periods. The data were fitted via Seasonal-Trend Decomposition using the Locally Estimated Scatterplot Smoothing (STL) method. Gray dashed lines indicate the periods of most stringent emission reductions, with response durations (in days) labeled in black. Blue, red, and orange numbers represent the relative changes (%) in AAQI and each IAQI for reduction vs. pre-reduction, recovery vs. reduction, and recovery vs. pre-reduction comparisons, respectively.

During the period of stringent emission reductions, Wuhan, a major urban center with intensive anthropogenic activities, experienced more pronounced and rapid pollution changes than the national average (Fig. 4). $PM_{2.5}$ and PM_{10} levels declined by 37% and 34%, respectively, with shorter response times of 35 and 38 days, indicating a stronger and faster particulate matter response to abrupt emission decreases. In contrast, O_3 levels increased sharply by 73%, about four times the national average, reflecting an intensified ozone formation response under substantially reduced NO_x emissions. NO_2 exhibited the largest decrease (47%) and the longest rebound period (65 days), consistent with the strong suppression of traffic and industrial emissions in the city. SO_2 and CO experienced moderate declines of 28% and 12%, respectively, with response times 2.3–2.4 times shorter than national averages. Overall, the AAQI in Wuhan decreased by 26% over an average recovery period of 61 days. Notably, the end of this recovery period, identified from satellite observations, closely matched the timing of the city's emission control easing, differing by only ~5 days, demonstrating the capability of space-based measurements to capture city-scale responses to emission interventions.

During the subsequent emission recovery phase, pollution levels in Wuhan partially rebounded, with NO_2 and PM_{10} increasing by 58% and 35%, respectively, approximately 2.2–2.3 times the corresponding national averages. $PM_{2.5}$ levels also rose by 24%, contrasting with the slight national decline. In comparison, O_3 exhibited a modest increase of 6%, while SO_2 and CO continued to decrease at rates similar to national trends. Consequently, the AAQI increased by 21%, reflecting the partial resumption of urban activities. Compared with national patterns, Wuhan experienced more pronounced and faster reductions in particulate matter and NO_2 during the emission reduction phase, a substantially larger O_3 enhancement, and a stronger rebound in NO_2 during the recovery phase, highlighting the effects of stricter local emission controls followed by a rapid return of anthropogenic emissions. Despite this rebound, pollution levels in Wuhan remained lower than pre-intervention levels: except for O_3, which increased by 69%, all other pollutants decreased by

https://doi.org/10.5194/egusphere-2026-891
Preprint. Discussion started: 18 February 2026
© Author(s) 2026. CC BY 4.0 License.

10–21%, resulting in an overall AAQI reduction of 11%. These results indicate that, although emissions partially recovered, lasting improvements in air quality persisted following the targeted emission control measures.

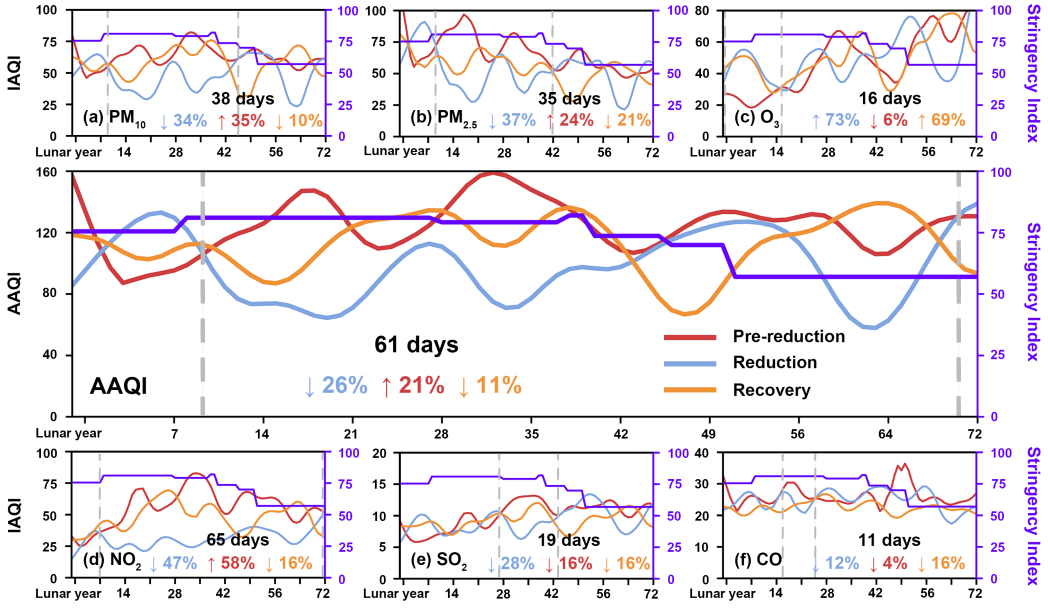

Figure 4. Response of air pollution to emission changes in Wuhan.
Time series of daily Aggregated Air Quality Index (AAQI) and Individual Air Quality Index (IAQI) (colored lines) for (a) PM_{10}, (b) $PM_{2.5}$, (c) O_3, (d) NO_2, (e) SO_2, and (f) CO, along with the Oxford Coronavirus Government Response Tracker (OxCGRT) stringency index (purple lines) as a proxy for emission reduction intensity during the pre-reduction (2019), reduction (2020), and recovery (2021–2022) periods in Wuhan, Hubei province, China. The data were fitted via Seasonal-Trend Decomposition using the Locally Estimated Scatterplot Smoothing (STL) method. Gray dashed lines indicate the periods of most stringent emission reductions, with response durations (in days) labeled in black. Blue, red, and orange numbers represent the relative changes (%) in AAQI and each IAQI for reduction vs. pre-reduction, recovery vs. reduction, and recovery vs. pre-reduction comparisons, respectively.

3.3 Fine-scale variations in air pollution across the domain

During the most stringent emission reduction period, only 13% and 9% of inhabited areas (population density > 1 person km^{-2}) and counties experienced an increase in PM_{10} compared to pre-reduction levels (Figs. 5a & S4a), primarily in the desert-dominated northwestern regions affected by enhanced dust events. In contrast, $PM_{2.5}$ decreased in 74% (76%) of inhabited areas

https://doi.org/10.5194/egusphere-2026-891
Preprint. Discussion started: 18 February 2026
© Author(s) 2026. CC BY 4.0 License.

(counties), particularly across the densely populated Northern China Plain, with reductions exceeding 50%. Significant declines in NO_2, SO_2, and CO were observed in 92% (98%), 85% (90%), and 72% (87%) of inhabited areas (counties), respectively, with the largest reductions occurring in urbanized regions of eastern China, especially Wuhan city, reflecting substantial suppression of direct emissions from transportation and industry. O_3 levels, conversely, increased in 76% (84%) of inhabited areas (counties), consistent with the spatial reduction of NO_2, which promotes ozone formation under a VOC-limited chemical regime. Overall, pollution levels improved markedly, with 73% of inhabited areas and 87% of counties showing decreases in the AAQI.

During the recovery period, fine-scale pollution patterns exhibited pronounced heterogeneity compared to the reduction period (Figs. 5b & S4b). PM_{10} increased in 87% (90%) of inhabited areas (counties), particularly in Northern and Southwestern China, while $PM_{2.5}$ worsened in approximately half of the domain (49% and 52% of inhabited areas and counties), mainly in urbanized southeastern regions, including the Yangtze and Pearl River Deltas. NO_2 experienced the largest increase, affecting 90% of inhabited areas and 96% of counties, including rural and less industrialized regions. This trend was particularly evident in Hubei province and surrounding areas, where increases exceeded 50%, reflecting the resumption of construction, transportation, and industrial activity. Moderate increases in SO_2 and CO (47% and 18% of inhabited areas, and 48% and 23% of counties) were primarily observed in specific industrial regions, suggesting a rebound in coal-dependent industries and partial relaxation of emission controls. O_3 rose in 55% (48%) of inhabited areas (counties), particularly in southern regions, likely due to high solar radiation and elevated precursor concentrations. While western regions generally experienced continued air quality improvements, central and eastern China saw noticeable declines. Overall, 72% of inhabited areas and 70% of counties showed AAQI increases, highlighting the impact of emission recovery on air pollution.

Comparing the recovery period to pre-reduction levels (Figs. 5c & S4c), PM_{10} worsened in 49% (43%) of the domain (counties), particularly in central-northern and southern regions, while $PM_{2.5}$ IAQI increased in 26% (24%) of areas (counties), mainly in densely populated and industrialized southern regions, reflecting the influence of resumed human activities. NO_2 increased in 32% (17%)

https://doi.org/10.5194/egusphere-2026-891
Preprint. Discussion started: 18 February 2026
© Author(s) 2026. CC BY 4.0 License.

of inhabited areas (counties), while SO_2 and CO showed smaller increases (16% (8%) and 13% (5%), respectively), indicating that emission controls on vehicles and certain industrial sectors remained effective in many areas. In contrast, O_3 rose sharply in 87% and 92% of inhabited areas and counties, particularly in southern and southeastern China, suggesting that elevated precursor concentrations (NO_x and VOCs) and favorable meteorological conditions enhanced ozone formation. Overall, air quality improved in 53% of inhabited areas and 66% of counties relative to pre-reduction levels, especially in densely populated central and eastern regions, although some areas experienced localized deteriorations.

https://doi.org/10.5194/egusphere-2026-891
Preprint. Discussion started: 18 February 2026
© Author(s) 2026. CC BY 4.0 License.

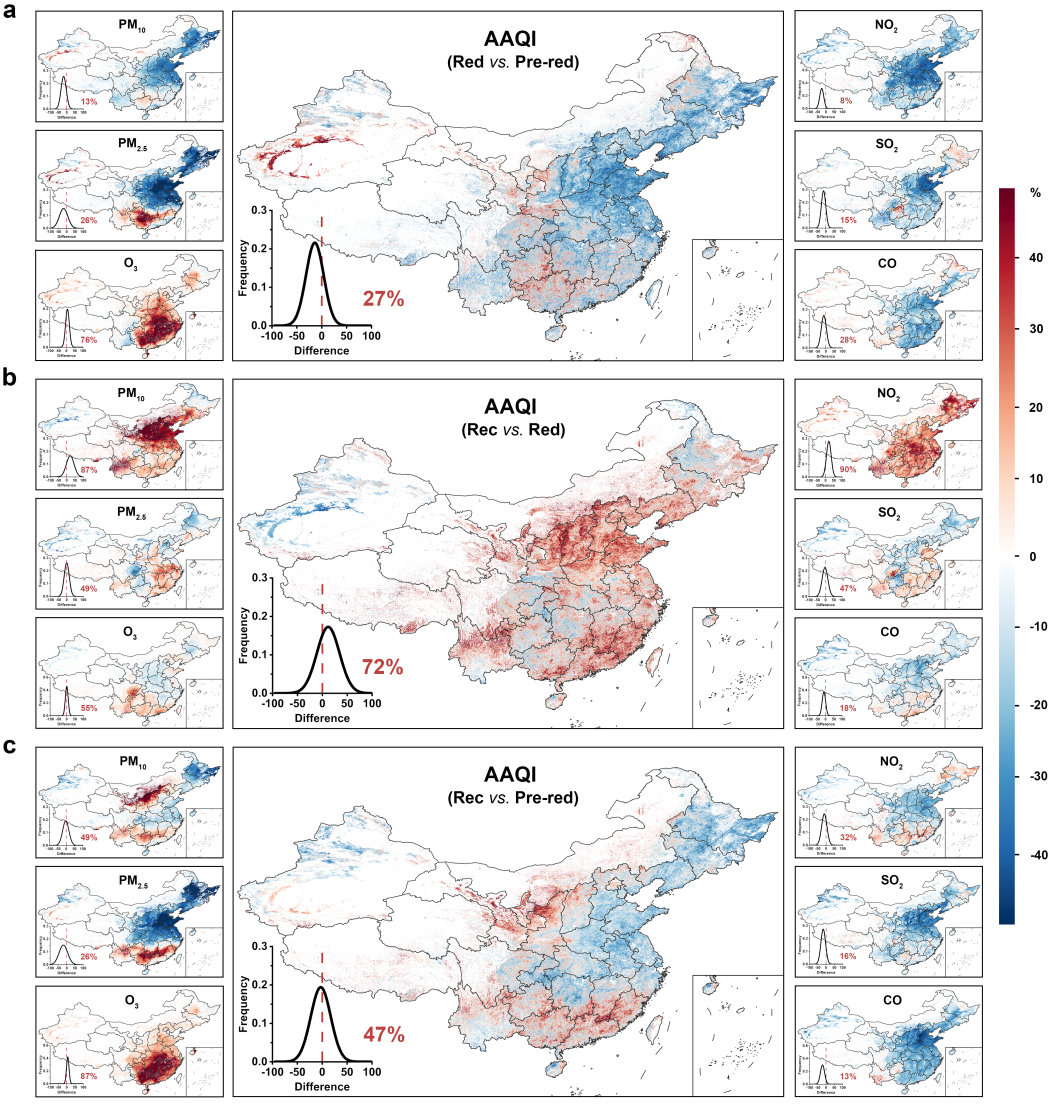

Figure 5. Fine-scale changes in air pollution across different emission-change eras in China. Spatial distributions of relative differences (%) in the Aggregated Air Quality Index (AAQI) and Individual Air Quality Index (IAQI) for PM_{10}, $PM_{2.5}$, O_3, NO_2, SO_2, and CO during the most stringent emission reduction periods, compared across three periods—(a) reduction vs. pre-reduction (2019 vs. 2019), (b) recovery vs. reduction (2021–2022 vs. 2020), and (c) recovery vs. pre-reduction (2021–2022 vs. 2019). Results are presented at 1 km^2 resolution for inhabited areas (population density > 1 person km^{-2}) across China. Lower-left plots display frequency histograms, with red numbers indicating the percentage of pixels showing worsened pollution levels due to emission recovery.

https://doi.org/10.5194/egusphere-2026-891
Preprint. Discussion started: 18 February 2026
© Author(s) 2026. CC BY 4.0 License.

3.4 Changes in polluted days across the first quarters

Leveraging the daily, gapless air pollutant dataset, we assessed changes in the number of days at different AAQI levels during the first quarter (January–March), which typically experiences severe pollution in China. For example, 40% (55%), 34% (44%), and 33% (48%) of inhabited areas (counties) experienced unhealthy pollution levels (AAQI > 100) for half of the quarter during the pre-reduction, reduction, and recovery periods, respectively (Figs. 6 & S5), respectively. Central and eastern China were particularly affected, with pollution exposure frequency exceeding three-fourths of the quarter. Compared to the pre-reduction period (Fig. S6), "Good" days (AAQI < 50) increased in 12% and 38% of inhabited areas and counties, primarily in southern China, while "Moderate" days (AAQI = 51–100) increased in 72% and 86% of areas, mostly in central and eastern regions. More notably, "Unhealthy for Sensitive Groups" (AAQI = 101–150) days decreased in 66% (62%) of inhabited areas (counties), especially in central and southeastern China, while reductions in "Unhealthy" (AAQI = 151–200) and "Very Unhealthy" days reached 85% (86%) and 93% (91%), with hotspots in the North China Plain. Overall, days with healthy pollution levels (AAQI < 100) increased in 76% of inhabited areas and 87% of counties (Figs. 6d & S5d), reflecting widespread improvements during the emission reduction period.

During the recovery period, "Moderate" days showed a mixed pattern, with increases in northern China but decreases in southern and eastern regions (amplitude > 20%), resulting in an overall increase in 65% of inhabited areas and 58% of counties (Fig. S7). In contrast, higher pollution levels—"Unhealthy for Sensitive Groups" and "Unhealthy" days—substantially increased in 59% (68%) and 50% (72%) of areas, mainly in central and southern China, consistent with the partial resumption of anthropogenic emissions. "Good" and "Very Unhealthy" categories showed minimal changes, whereas "Hazardous" days (AAQI = 301–500) increased in 57% (50%) of inhabited areas (counties). These patterns indicate an overall worsening of pollution levels during emission recovery (Figs. 6e, S5e), with unhealthy days (AAQI > 100) rising in 63% and 71% of inhabited areas and counties.

Comparing the recovery to the pre-reduction period (Fig. S8), "Good" days remained similar to the reduction period, with minimal changes in southern regions. "Moderate" days increased in 63% and 73% of inhabited areas and counties, with widespread growth across central and southern

https://doi.org/10.5194/egusphere-2026-891
Preprint. Discussion started: 18 February 2026
© Author(s) 2026. CC BY 4.0 License.

China, especially in Hubei and surrounding areas, while declines were observed in southern provinces such as Guangdong and Guangxi. Continuous reductions were observed in "Unhealthy for Sensitive Groups," "Unhealthy," and "Very Unhealthy" days across 52% (43%), 73% (68%), and 82% (79%) of areas (counties), particularly in the Shandong Peninsula and nearby regions. Meanwhile, "Hazardous" days showed minor spatial changes (<5%). These results suggest that, although emissions partially recovered, overall pollution levels generally improved relative to pre-reduction levels (Figs. 6f, S5f), with a pronounced north–south contrast—healthy days increased in northern China but decreased in southern regions (65% vs. 35% of inhabited areas, 73% vs. 27% of counties).

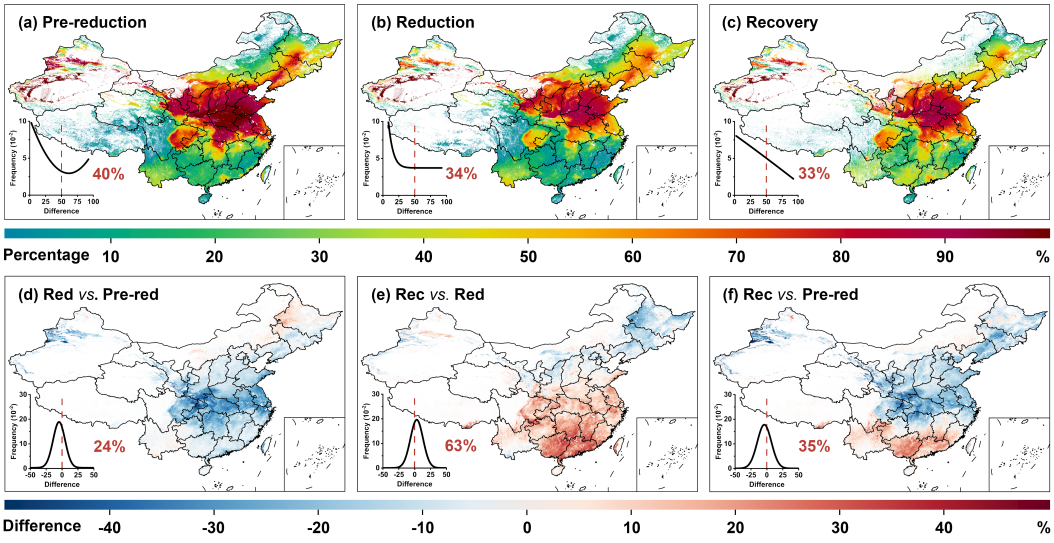

Figure 6. Changes in unhealthy days across different emission-change eras in China. Spatial distribution of the percentage of days exceeding unhealthy pollution levels [i.e., falling outside the Good (AAQI = 0–50) and Moderate (51–100) categories] during the first quarter (January–March) for the (a) pre-reduction (2019), (b) reduction (2020), and (c) recovery (2021–2022) periods, along with their differences (%) for the following comparisons: (d) reduction vs. pre-reduction, (e) recovery vs. reduction, and (f) recovery vs. pre-reduction. Results are presented at 1 km^2 resolution for inhabited areas (population density > 1 person km^{-2}) across China.

3.5 Drivers of major air pollutant changes with XAI

Using eXplainable Artificial Intelligence (XAI), we examined the drivers of changes in $PM_{2.5}$ and O_3 concentrations across the pre-reduction (2019), reduction (2020), and recovery (2021–2022)

https://doi.org/10.5194/egusphere-2026-891
Preprint. Discussion started: 18 February 2026
© Author(s) 2026. CC BY 4.0 License.

periods. For $PM_{2.5}$, population-weighted concentrations declined by 32% during the reduction period, primarily driven by a 22% decrease in anthropogenic emissions (Fig. 7a). Sharp emission reductions from industrial activities and transportation led to marked decreases in particulate matter and its precursors. Meteorological conditions contributed a secondary yet important role, accounting for an additional 10% reduction through enhanced dispersion and increased precipitation. During the recovery period, $PM_{2.5}$ stabilized at 40.5 μg m^{-3}, with minor changes attributed to meteorology (1% reduction) and a modest rebound in anthropogenic emissions (4% increase). These results highlight the dominant role of human-driven emissions in controlling $PM_{2.5}$ levels, even as pollution reductions persisted after the emission control measures.

For O_3, the response differed: during the reduction period, population-weighted concentrations increased by 18% relative to pre-reduction levels, largely due to meteorological factors (15%) and partially to emission changes (3%) (Fig. 7b). This increase reflects the complex photochemical response to reduced NO_x emissions during lockdowns: Lower NOx emissions during the reduction period decreased O_3 titration in urban areas, resulting in higher ambient O_3 through non-linear photochemical processes. During the recovery period, O_3 remained elevated at 84.6 μg m^{-3}, with negligible additional contributions from meteorology or anthropogenic emissions. These findings underscore the dominant influence of meteorology on O_3 variations, modulated by chemical responses to emission reductions.

Considering regional differences north and south of the Qinling-Huaihe Line, we conducted separate XAI analyses (Fig. 7c-f). During the reduction period, $PM_{2.5}$ changes mirrored national trends, dominated by anthropogenic emission decreases (23% in northern China and 11% in southern China), while O_3 variations were primarily meteorology-driven (12% and 13%, respectively). In the recovery period, $PM_{2.5}$ and O_3 continued to decline in northern China by 5% and 6%, with anthropogenic factors dominating, whereas both pollutants increased in southern China. In this region, $PM_{2.5}$ increases were driven by both human activities and meteorology, while O_3 rises were largely meteorology-driven, influenced by high temperature and humidity.

At the city scale, Wuhan exhibited distinctive trends (Fig. 7g-h). During the reduction period, $PM_{2.5}$ decreased by 37%, mainly due to human emission reductions (22%), whereas O_3 increased

https://doi.org/10.5194/egusphere-2026-891
Preprint. Discussion started: 18 February 2026
© Author(s) 2026. CC BY 4.0 License.

by 40%, dominated by meteorological factors. During the recovery period, $PM_{2.5}$ rebounded by 26%, largely driven by meteorology (~16%), while O_3 decreased by 5%, with meteorology again as the primary driver. These XAI results are consistent with traditional Multiple Linear Regression (MLR) analyses (Fig. S9) but provide a more nuanced understanding of non-linear interactions between pollutants and their drivers at national, regional, and urban scales.

Overall, the results highlight the contrasting responses of O_3 and $PM_{2.5}$ to changes in emissions: reductions in primary pollutants yield clear benefits for particulate matter but can lead to increased O_3 through complex photochemistry. This underscores the need for balanced emission control strategies that simultaneously address primary and secondary pollutants, especially in densely populated and industrialized regions. The analysis further shows that while emission reductions can rapidly lower pollution levels, adaptive regulatory frameworks are essential for the sustainable management of both $PM_{2.5}$ and O_3.

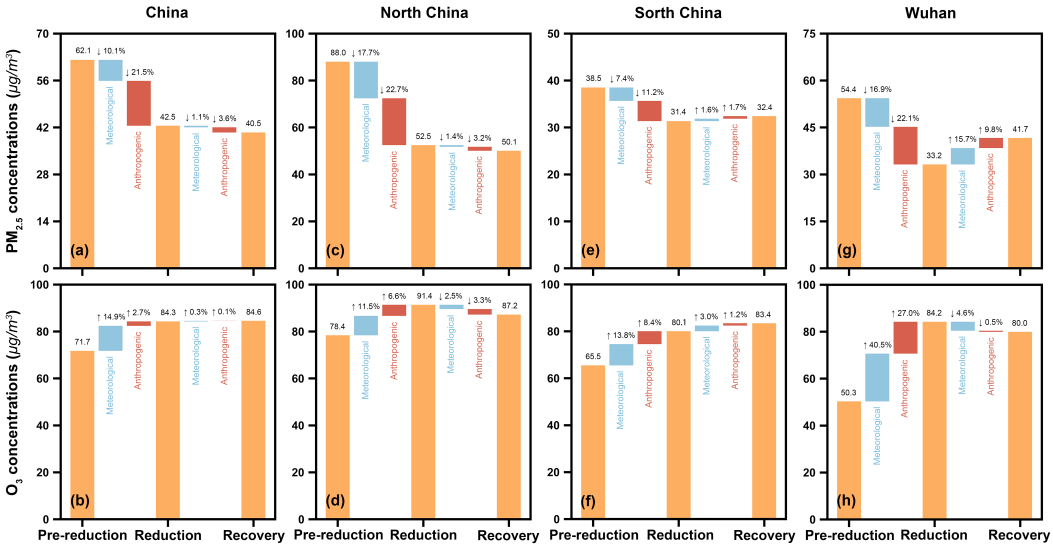

Figure 7. Drivers of air pollution variations across different emission-change eras. Influencing factors driving changes in ambient $PM_{2.5}$ and O_3 pollution during the most stringent emission reduction period—from the pre-reduction (2019) to the reduction (2020) and recovery (2021–2022) periods—in (a & b) China, (c & d) Northern China, (e & f) Southern China, and (g & h) Wuhan city, Hubei province, using eXplainable Artificial Intelligence (XAI). The blue and red bars represent the contributions of meteorological conditions and anthropogenic emissions, respectively.

https://doi.org/10.5194/egusphere-2026-891
Preprint. Discussion started: 18 February 2026
© Author(s) 2026. CC BY 4.0 License.

4. Conclusions

Previous studies of air pollution changes in China have largely focused on regional scales, individual pollutants, or the pre-reduction and reduction periods, with uneven ground-monitor coverage limiting fine-scale, nationwide assessment of post-reduction pollution levels. To address these gaps, we developed a uniform deep learning–based framework to generate a daily, gapless dataset at 1 km² resolution for six conventional air pollutants across China from 2019 to 2022. The resulting daily estimates show strong agreement with over 2.2 million ground-based observations, achieving high accuracy (PM_{10}: CV-R^2 = 0.92, RMSE = 16.87 μg m^{-3}; $PM_{2.5}$: 0.93, 7.58 μg m^{-3}; O_3: 0.94, 11.48 μg m^{-3}; NO_2: 0.87, 6.34 μg m^{-3}; SO_2: 0.79, 3.93 μg m^{-3}; CO: 0.80, 0.18 mg m^{-3}), enabling robust multi-pollutant analyses at pixel- and county-scales.

We characterized pollution evolution across the pre-reduction, reduction, and recovery periods, capturing distinct response times to abrupt emission changes (17–47 days). During the reduction period, air quality improved substantially across China, with $PM_{2.5}$ and PM_{10} declining in 76% and 91% of counties, NO_2, SO_2, and CO decreasing in 98%, 90%, and 87% of counties, respectively, and overall AAQI improving in 87% of counties, despite O_3 increases in 84% of counties. In contrast, the recovery period showed a widespread rebound of air pollution, with NO_2, PM_{10}, and $PM_{2.5}$ increasing in 96%, 90%, and 52% of counties, respectively, leading to AAQI deterioration in 70% of counties as economic activity resumed. Nevertheless, relative to pre-reduction conditions, most primary pollutants (PM_{10}, $PM_{2.5}$, NO_2, SO_2, and CO) remained lower in 57–95% of counties, resulting in net AAQI improvements in 66% of counties, despite a pervasive increase in O3 across 92% of counties. These transitions produced pronounced wave-like changes in healthy days (AAQI < 100) during the most pollution-sensitive first quarter (January–March), highlighting the combined roles of emission controls, economic recovery, and seasonal processes in shaping post-reduction pollution levels.

Explainable AI (XAI) analysis revealed that, at the national scale, $PM_{2.5}$ variations were dominated by reductions in anthropogenic emissions (22% during the reduction period), whereas O_3 changes were primarily driven by meteorology (15% during the reduction period) and non-linear photochemical responses to NO_x reductions. In Wuhan, $PM_{2.5}$ declined during the reduction period

https://doi.org/10.5194/egusphere-2026-891
Preprint. Discussion started: 18 February 2026
© Author(s) 2026. CC BY 4.0 License.

primarily due to anthropogenic reductions (~22%) but rebounded during recovery, largely driven by meteorological factors (~16%), while O_3 remained meteorologically controlled, increasing 40% during reduction and decreasing 5% during recovery. Our study provides high-resolution evidence of pollution evolution in China and underscores the need for coordinated, multi-pollutant, mechanism-oriented management strategies that address both primary and secondary pollutants.

Data availability

The generated high-resolution and high-quality datasets of ambient air pollutants for China (CHAP) are publicly available at https://zenodo.org/communities/chap/.

Acknowledgments

This work was supported by the National Key Technology and Development Program of Corps (2025AA001).

Author Contributions

JW designed the study. ZY conducted the research. JW and ZY drafted the manuscript. CF assisted with data analysis. JG, HL, and JW reviewed and edited the paper.

Competing interests

The authors declare no competing interests.

References

Antwarg, L., Miller, R. M., Shapira, B., and Rokach, L.: Explaining anomalies detected by autoencoders using Shapley Additive Explanations, Expert Systems with Applications, 186, 115736, https://doi.org/10.1016/j.eswa.2021.115736, 2021.

Bhatti, U. A., Zeeshan, Z., Nizamani, M. M., Bazai, S., Yu, Z., and Yuan, L.: Assessing the change of ambient air quality patterns in Jiangsu Province of China pre-to post-COVID-19, Chemosphere, 288, 132569, https://doi.org/10.1016/j.chemosphere.2021.132569, 2022.

Cersosimo, A., Serio, C., and Masiello, G.: TROPOMI NO_2 Tropospheric Column Data: Regridding to 1 km Grid-Resolution and Assessment of their Consistency with In Situ Surface Observations, 10.3390/rs12142212, 2020.

https://doi.org/10.5194/egusphere-2026-891
Preprint. Discussion started: 18 February 2026
© Author(s) 2026. CC BY 4.0 License.

660 Cheng, F., Li, Z., Yang, Z., Li, R., Wang, D., Jia, A., Li, K., Zhao, B., Wang, S., Yin, D., Li, S., Xue, W., Cribb, M., and Wei, J.: First retrieval of 24-hourly 1-km-resolution gapless surface ozone (O_3) from space in China using artificial intelligence: Diurnal variations and implications for air quality and phytotoxicity, Remote Sensing of Environment, 316, 114482, 10.1016/j.rse.2024.114482, 2025.

665 Cleveland, R. B., Cleveland, W. S., McRae, J. E., and Terpenning, I. J. J. o. S.: STL: A seasonal-trend decomposition, 6, 3-73, 1990.

Cooper, M. J., Martin, R. V., Hammer, M. S., Levelt, P. F., Veefkind, P., Lamsal, L. N., Krotkov, N. A., Brook, J. R., and McLinden, C. A.: Global fine-scale changes in ambient NO_2 during COVID-19 lockdowns, Nature, 601, 380-387, 2022.

670 Feng, T., Du, H., Lin, Z., Chen, X., Chen, Z., and Tu, Q.: Green recovery or pollution rebound? Evidence from air pollution of China in the post-COVID-19 era, Journal of Environmental Management, 324, 116360, https://doi.org/10.1016/j.jenvman.2022.116360, 2022.

Geng, G., Liu, Y., Liu, Y., Liu, S., Cheng, J., Yan, L., Wu, N., Hu, H., Tong, D., Zheng, B., Yin, Z., He, K., and Zhang, Q.: Efficacy of China's clean air actions to tackle $PM_{2.5}$ pollution

675 between 2013 and 2020, Nature Geoscience, 17, 987-994, 10.1038/s41561-024-01540-z, 2024.

Guo, Q., Wang, Z., He, Z., Li, X., Meng, J., Hou, Z., and Yang, J.: Changes in Air Quality from the COVID to the Post-COVID Era in the Beijing-Tianjin-Tangshan Region in China, Aerosol and Air Quality Research, 21, 210270, 10.4209/aaqr.210270, 2021.

680 Hersbach, H., Bell, B., Berrisford, P., Hirahara, S., Horányi, A., Muñoz-Sabater, J., Nicolas, J., Peubey, C., Radu, R., Schepers, D., Simmons, A., Soci, C., Abdalla, S., Abellan, X., Balsamo, G., Bechtold, P., Biavati, G., Bidlot, J., Bonavita, M., De Chiara, G., Dahlgren, P., Dee, D., Diamantakis, M., Dragani, R., Flemming, J., Forbes, R., Fuentes, M., Geer, A., Haimberger, L., Healy, S., Hogan, R. J., Hólm, E., Janisková, M., Keeley, S., Laloyaux, P.,

685 Lopez, P., Lupu, C., Radnoti, G., de Rosnay, P., Rozum, I., Vamborg, F., Villaume, S., and Thépaut, J.-N.: The ERA5 global reanalysis, Quarterly Journal of the Royal Meteorological Society, 146, 1999-2049, 2020.

Hu, J., Ying, Q., Wang, Y., and Zhang, H.: Characterizing multi-pollutant air pollution in China: Comparison of three air quality indices, Environment International, 84, 17-25, 2015.

690 Kyrkilis, G., Chaloulakou, A., and Kassomenos, P. A.: Development of an aggregate Air Quality

https://doi.org/10.5194/egusphere-2026-891
Preprint. Discussion started: 18 February 2026
© Author(s) 2026. CC BY 4.0 License.

Index for an urban Mediterranean agglomeration: Relation to potential health effects, Environment International, 33, 670-676, 2007.

Li, Z.: Extracting spatial effects from machine learning model using local interpretation method: An example of SHAP and XGBoost, Computers, Environment and Urban Systems, 96, 101845, 2022.

Liu, Y., Wang, T., Stavrakou, T., Elguindi, N., Doumbia, T., Granier, C., Bouarar, I., Gaubert, B., and Brasseur, G. P.: Diverse response of surface ozone to COVID-19 lockdown in China, Science of The Total Environment, 789, 147739, 2021.

MEE: Ministry of Ecology and Environment (MEE), 2018. Revision of the Ambien air quality standards (GB 3095–2012) (in Chinese), 2018.

Muñoz-Sabater, J., Dutra, E., Agustí-Panareda, A., Albergel, C., Arduini, G., Balsamo, G., Boussetta, S., Choulga, M., Harrigan, S., Hersbach, H., Martens, B., Miralles, D. G., Piles, M., Rodríguez-Fernández, N. J., Zsoter, E., Buontempo, C., and Thépaut, J. N.: ERA5-Land: a state-of-the-art global reanalysis dataset for land applications, Earth Syst. Sci. Data, 13, 4349-4383, 2021.

Venter, Z. S., Aunan, K., Chowdhury, S., and Lelieveld, J.: COVID-19 lockdowns cause global air pollution declines, Proceedings of the National Academy of Sciences, 117, 18984-18990, 10.1073/pnas.2006853117 2024/12/29 doi: 10.1073/pnas.2006853117, 2020.

Wang, Q. and Yang, X.: How do pollutants change post-pandemic? Evidence from changes in five key pollutants in nine Chinese cities most affected by the COVID-19, Environmental Research, 197, 111108, https://doi.org/10.1016/j.envres.2021.111108, 2021.

Wang, X. and Zhang, R.: How Did Air Pollution Change during the COVID-19 Outbreak in China?, Bulletin of the American Meteorological Society, 101, E1645-E1652, 2020.

Wei, J., Li, Z., Wang, J., Li, C., Gupta, P., and Cribb, M.: Ground-level gaseous pollutants (NO_2, SO_2, and CO) in China: daily seamless mapping and spatiotemporal variations, Atmos. Chem. Phys., 23, 1511-1532, 2023a.

Wei, J., Li, Z., Lyapustin, A., Sun, L., Peng, Y., Xue, W., Su, T., and Cribb, M.: Reconstructing 1-km-resolution high-quality $PM_{2.5}$ data records from 2000 to 2018 in China: spatiotemporal variations and policy implications, Remote Sensing of Environment, 252, 112136, 2021a.

Wei, J., Li, Z., Xue, W., Sun, L., Fan, T., Liu, L., Su, T., and Cribb, M.: The ChinaHighPM$_{10}$ dataset: generation, validation, and spatiotemporal variations from 2015 to 2019 across China.

https://doi.org/10.5194/egusphere-2026-891
Preprint. Discussion started: 18 February 2026
© Author(s) 2026. CC BY 4.0 License.

Environment International, 146, 106290. https://doi.org/10.1016/j.envint.2020.106290, 2021b.

Wei, J., Wang, Z., Li, Z., Li, Z., Pang, S., Xi, X., Cribb, M., and Sun, L.: Global aerosol retrieval over land from Landsat imagery integrating Transformer and Google Earth Engine, Remote Sensing of Environment, 315, 114404, https://doi.org/10.1016/j.rse.2024.114404, 2024.

Wei, J., Li, Z., Li, K., Dickerson, R. R., Pinker, R. T., Wang, J., Liu, X., Sun, L., Xue, W., and Cribb, M.: Full-coverage mapping and spatiotemporal variations of ground-level ozone (O_3) pollution from 2013 to 2020 across China, Remote Sensing of Environment, 270, 112775, https://doi.org/10.1016/j.rse.2021.112775, 2022a.

Wei, J., Li, Z., Lyapustin, A., Wang, J., Dubovik, O., Schwartz, J., Sun, L., Li, C., Liu, S., and Zhu, T.: First close insight into global daily gapless 1 km $PM_{2.5}$ pollution, variability, and health impact, Nature Communications, 14, 8349, https://doi.org/10.1038/s41467-023-43862-3, 2023b.

Wei, J., Wang, J., Li, Z., Kondragunta, S., Anenberg, S., Wang, Y., Zhang, H., Diner, D., Hand, J., Lyapustin, A., Kahn, R., Colarco, P., Da Silva, A., and Ichoku, C.: Long-term mortality burden trends attributed to black carbon and $PM_{2.5}$ from wildfire emissions across the continental USA from 2000 to 2020: a deep learning modelling study, The Lancet Planetary Health, 7, e963-e975, https://doi.org/10.1016/S2542-5196(23)00235-8, 2023c.

Wei, J., Liu, S., Li, Z., Liu, C., Qin, K., Liu, X., Pinker, R. T., Dickerson, R. R., Lin, J., Boersma, K. F., Sun, L., Li, R., Xue, W., Cui, Y., Zhang, C., and Wang, J.: Ground-Level NO_2 Surveillance from Space Across China for High Resolution Using Interpretable Spatiotemporally Weighted Artificial Intelligence, Environmental Science & Technology, 56, 9988-9998, https://doi.org/10.1021/acs.est.2c03834, 2022b.

Wei, J., Li, Z., Chen, X., Li, C., Sun, Y., Wang, J., Lyapustin, A., Brasseur, G. P., Jiang, M., Sun, L., Wang, T., Jung, C. H., Qiu, B., Fang, C., Liu, X., Hao, J., Wang, Y., Zhan, M., Song, X., and Liu, Y.: Separating Daily 1 km $PM_{2.5}$ Inorganic Chemical Composition in China since 2000 via Deep Learning Integrating Ground, Satellite, and Model Data, Environmental Science & Technology, 57, 18282-18295, https://doi.org/10.1021/acs.est.3c00272, 2023d.

Yang, Z., Li, Z., Cheng, F., Lv, Q., Li, K., Zhang, T., Zhou, Y., Zhao, B., Xue, W., and Wei, J.: Two-decade surface ozone (O_3) pollution in China: Enhanced fine-scale estimations and environmental health implications, Remote Sensing of Environment, 317, 114459,

https://doi.org/10.5194/egusphere-2026-891
Preprint. Discussion started: 18 February 2026
© Author(s) 2026. CC BY 4.0 License.

https://doi.org/10.1016/j.rse.2024.114459, 2025.

Zhu, J., Chen, L., Liao, H., Yang, H., Yang, Y., and Yue, X.: Enhanced $PM_{2.5}$ Decreases and O_3 Increases in China During COVID-19 Lockdown by Aerosol-Radiation Feedback, Geophysical Research Letters, 48, e2020GL090260, 2021.